



## Investigation of a Monturaqui Impactite by Means of Bi-Modal X-ray and Neutron Tomography

Fedrigo, Anna; Marstal, Kasper; Koch, Christian Bender; Dahl, Vedrana Andersen; Dahl, Anders Bjorholm; Lyksborg, Mark; Gundlach, Carsten; Ott, Frédéric; Strobl, Markus

*Published in:*  
Journal of Imaging

*DOI:*  
[10.3390/jimaging4050072](https://doi.org/10.3390/jimaging4050072)

*Publication date:*  
2018



*Document version*  
Publisher's PDF, also known as Version of record

*Document license:*  
[CC BY](#)

*Citation for published version (APA):*  
Fedrigo, A., Marstal, K., Koch, C. B., Dahl, V. A., Dahl, A. B., Lyksborg, M., ... Strobl, M. (2018). Investigation of a Monturaqui Impactite by Means of Bi-Modal X-ray and Neutron Tomography. *Journal of Imaging*, 4(5), [72].  
<https://doi.org/10.3390/jimaging4050072>

Article

# Investigation of a Monturaqui Impactite by Means of Bi-Modal X-ray and Neutron Tomography

Anna Fedrigo <sup>1,2,3,\*</sup> , Kasper Marstal <sup>3,4</sup>, Christian Bender Koch <sup>5</sup>, Vedrana Andersen Dahl <sup>3</sup>, Anders Bjorholm Dahl <sup>3</sup>, Mark Lyksborg <sup>3</sup>, Carsten Gundlach <sup>6</sup>, Frédéric Ott <sup>7</sup> and Markus Strobl <sup>2,8,9</sup> 

<sup>1</sup> Science and Technology Facility Council, ISIS Neutron Source, Didcot OX11 0QX, UK

<sup>2</sup> European Spallation Source ESS ERIC, SE-221 00 Lund, Sweden; markus.strobl@psi.ch

<sup>3</sup> DTU Compute, DK-2800 Kgs Lyngby, Denmark; kkmars@dtu.dk (K.M.); vand@dtu.dk (V.A.D.); abda@dtu.dk (A.B.D.); Mark\_Lyksborg@hotmail.com (M.L.)

<sup>4</sup> ERASMUS MC, Biomedical Imaging Group, 3000 CA Rotterdam, The Netherlands

<sup>5</sup> Department of Chemistry, University of Copenhagen, 2100 Copenhagen, Denmark; cbk@chem.ku.dk

<sup>6</sup> DTU Physics, 2800 Kgs Lyngby, Denmark; cagu@fysik.dtu.dk

<sup>7</sup> Laboratoire Léon Brillouin, CEA-CNRS, 91191 Gif-sur-Yvette CEDEX, France; frederic.ott@cea.fr

<sup>8</sup> Nano-Science Centre, Niels Bohr Institute, University of Copenhagen, 2100 Copenhagen, Denmark

<sup>9</sup> Paul Scherrer Institut, 5232 Villigen, Sweden

\* Correspondence: anna.fedrigo@stfc.ac.uk; Tel.: +44-123-544-5900

Received: 21 March 2018; Accepted: 12 May 2018; Published: 18 May 2018



**Abstract:** X-ray and neutron tomography are applied as a bi-modal approach for the 3D characterisation of a Monturaqui impactite formed by shock metamorphism during the impact of an iron meteorite with the target rocks in the Monturaqui crater (Chile). The particular impactite exhibits structural heterogeneities on many length scales: its composition is dominated by silicate-based glassy and crystalline materials with voids and Fe/Ni-metal and oxihydroxides particles generally smaller than 1 mm in diameter. The non-destructive investigation allowed us to apply a novel bi-modal imaging approach that provides a more detailed and quantitative understanding of the structural and chemical composition compared to standard single mode imaging methods, as X-ray and neutron interaction with matter results in different attenuation coefficients with a non-linear relation. The X-ray and neutron data sets have been registered, and used for material segmentation, porosity and metallic content characterization. The bimodal data enabled the segmentation of a large number of different materials, their morphology as well as distribution in the specimen including the quantification of volume fractions. The 3D data revealed an evaporite type of material in the impactite not noticed in previous studies. The present study is exemplary in demonstrating the potential for non-destructive characterisation of key features of complex multi-phase objects such as impactites.

**Keywords:** neutron imaging; X-ray imaging; multimodal imaging; bimodal imaging; computed tomography; impactite; Monturaqui

## 1. Introduction

X-ray computed tomography (CT) has long demonstrated its potential as a non-destructive analysis and visualisation method in geoscience, with applications extending from palaeontology, to soil research, oil and gas production, among others [1–3]. X-ray CT has been complemented by neutron radiography and neutron tomography, expanding the range of applications to e.g., the study of denser materials and larger samples volumes, and to samples with light elements dispersed in

a matrix of heavy elements [4–7]. The application of multimodal imaging has gained in popularity in the recent years and researchers have come to realize that the complementary abilities of these two well-established imaging modalities could be exploited more efficiently by using them in tandem. This has even led to the implementation/design of simultaneous X-ray and neutron imaging instruments, such as ICON at the neutron spallation source SINQ (CH) [8], NeXT system at the NIST Centre for Neutron Research (USA) [9], and the NeXT-Grenoble at the ILL reactor in Grenoble (FR) [10]. The combined use of X-rays and neutrons provides additional element-dependent information since the physics of radiation interaction with the elements constituting the sample differs [11]: X-rays interact mainly with the electrons of an atom (the more electrons an atom has the higher the probability of interaction), whereas neutrons are electrically neutral particles that interact with the atomic nuclei. Neutrons are very sensitive to some light atoms, most notably hydrogen which has a scattering cross-section typically one order of magnitude larger than that of other atoms [11]. Therefore, water and hydroxyls associated with minerals show low contrast when using X-rays, but can readily be visualized by neutrons. Dense materials, including most metals, instead exhibit strong X-ray attenuation but are relatively transparent when using neutrons [11]. In favourable cases, neutron imaging helps even to differentiate between isotopes or neighbouring elements of the periodic table [11].

Here, we present a 3D imaging investigation of a weathered impactite rock from the Monturaqui meteorite impact crater in northern Chile. The impactite is a shock-metamorphosed rock resulting from the collision of an iron meteorite and terrestrial silicate rocks. Such collisions cause irreversible changes in the materials due to the formation and propagation of a shock wave in both the impactor and the target. For terrestrial planets, the impact can induce pressures up to several 100 GPa and temperatures up to thousands of degrees Celsius [12].

A frequently observed feature of impactites formed by iron meteorites is the incorporation of fragments and spherules of the meteorite into the impactite glass. Pores, vesicles and cracks are also a prominent characteristic of impactites. Both metallic spherules and vesicles typically range in size from  $\mu\text{m}$  to cm, therefore it is possible to resolve these objects at most sizes. Cracks and pores in the impactite may at later stages allow oxygen and water access to the metal, resulting in corrosion and the internal transport and precipitation of corrosion products in cracks and voids. Since weathering products typically contain hydrogen—or are associated with water adsorbed to surfaces—they will be particularly distinct in neutron imaging.

The resulting impactite rocks represent chemical disequilibrium products where vitreous phases are mixed with shocked and unshocked lithic fragments and vaporised/condensed metal deriving from the meteorite, forming vesiculated heterogeneous aggregates. While previous 2D studies [13] have identified most of the constituents in the impactite, major shortcomings exist concerning quantification of the constituents and their relative position within the impactite. This information is prerequisite in studies of the interactions of the constituents during impactite formation and weathering and would ultimately give a detailed understanding of the impactite formation processes.

Unlike terrestrial matter, iron meteorites—and consequently the corresponding crater and its surrounding ejecta blanket—are relatively rich in platinum-group metals (e.g., Ir, Pt, Re) which are used as markers to identify terrestrial impact craters [14]. Iridium concentration anomalies show a strong correlation to meteoritic events [15,16], but they are not truly unequivocal factors. Instead, the co-occurrence of a vesiculated partly melted matrix (the impactite rock) and metallic projectile droplets of meteoric origin (FeNi micro-spherules) represent a peculiar feature specific to meteoritic events only [17].

The present case-study shows the extent of information that can be elicited through a non-invasive approach combining X-ray and neutron tomography. This work represents a novel example where these two techniques have been methodically correlated for analysis. The focus of this study is to quantify and differentiate the different lithologies. Since the theoretical X-ray and neutron attenuation coefficients of a mineral can be calculated, it is possible to make predictions concerning its visibility and detectability inside the reconstructed tomographic volumes. X-ray CT, with its relatively high

resolution and contrast, was applied for morphological studies (e.g., porosity) and quantification of metallic spherules. Neutrons were used as they provide high contrast for hydrogen in metal oxides and for platinum-group and noble metals (e.g., Cu, Re, Ir, Pt, Au), which are originally present as trace elements in iron meteorites.

Both techniques provide important 3D information on the internal structure of materials. Results obtained are compared to current literature and to results obtained from standard destructive analysis on analogous Monturaqui impactites.

This study has a two-fold aim. First, it is well suited to exploit approaches of bi-modal visualisation and analyses to a detailed, multi-component object, as a model system for corresponding studies and strategies. Second, the study aims to investigate the full potential of non-destructive imaging applied to this class of geological samples, to help inform future studies and build an understanding of where and how far non-destructive imaging can replace destructive investigations.

## 2. Materials and Methods

### 2.1. Monturaqui Crater and Impactite

Monturaqui is an old ( $663,000 \pm 90,000$  years [18]) small-sized crater (360–380 m across and 21–39 m deep) situated at an altitude of 3100 m in the Atacama Desert region of the Andes [19]. The region is currently one of the most arid in the world, with an annual precipitation of less than 1 mm [20], generally limiting the extent of water-based weathering. The target rocks of the impact comprise of granite rock, overlaid by a thin sheet of ignimbrite from adjacent volcanoes [19]. Ignimbrites are pyroclastic rocks containing angular clasts of ash and lapilli tuff ranging in size from a few cm to over 50 cm. The ash and tuff contain pumice clasts as well as crystals of plagioclase feldspar, quartz, and biotite [21]. The Monturaqui impact event has been modelled [22] estimating an impactor of  $\sim 14.92$  m in diameter with a density of  $6.31 \text{ g/cm}^3$ . The energy of the impact produced  $\sim 6.8 \times 10^6 \text{ m}^3$  of impact melt of  $\sim 2.63 \text{ g/cm}^3$ , material that was ejected as far as 11.49 km from the impact.

While individual metallic fragments detached from the meteorite and deposited on the surface were almost completely transformed over the years into fine grained iron (oxi)hydroxides (mainly goethite and maghemite), impactites host a small—but characteristic—volume of particles of metallic Fe-Ni (some having additional FeS) embedded in glass and thereby protected from corrosion [23].

Since the discovery of the crater in 1962, Monturaqui impactites have been extensively studied by destructive methods: petrography in particular, but also scanning electron microscope (SEM), electron microprobe (EMP) analysis, X-ray fluorescence (XRF), inductively coupled plasma mass spectrometry (ICP-MS) analysis, and Mössbauer spectroscopy [18,23–28]. These analyses demonstrated the occurrence of FeNi spherules and related weathering oxides, and showed different structural components derived from the original target rocks. The glass component of the Monturaqui impactites is formed from the non-modal melting of granitic minerals, the melting of the ignimbrite, or a combination of the two [18], and possibly the addition of Fe and Ni from the meteorite. From the analysis of the melted minerals and of the planar deformation features of plagioclase and quartz grains, the impact temperatures were estimated to be  $<1700^\circ\text{C}$  and pressures  $\sim 45\text{--}55 \text{ GPa}$  [29].

Monturaqui impactites are vesiculated and mainly of sub-rounded morphology, in part appearing as though formed by the cladding of different materials, but also exhibiting evidence of explosive disruption (part of vesicles constituting the exterior surfaces, see Figure 1). They are heterogeneous in colour and texture. For this study we have selected a piece of Monturaqui impactite (collected by Dr. V.F. Buchwald) of approximately  $5 \times 3 \times 3 \text{ cm}^3$  (see Figure 1). This piece of impactite exhibits the characteristic vesicles, oxides, and metallic inclusions.

The metallic spheres are generally scattered in the impactite glass and can range in size from less than  $1 \mu\text{m}$  to more than 2 mm diameter. A previous study [30] from a CT reconstruction of a piece of impact melt estimated the volume occupied by the spherules to  $\sim 4.6\%$  of the total. The spherules have a higher Ni content compared to the bulk composition of the iron meteorite [23,25], but the composition



varies. The ratio of Ni to Fe ranges from 5–10% Ni (as kamacite), up to 20–74% Ni (as taenite) [25,28]. Ni-rich spherules are more resistant to corrosion [31]. The spherules are also enriched in Co with respect to the meteorite [15]. Co is ~3% of Ni or higher [30], 2 to 10 times more than the original meteorite [25]. In addition, spherules can also contain varying amounts of sulphur, in the form of interstitial troilite (FeS) and pyrrhotite (Fe<sub>(1-x)</sub>S). This sulphur is very likely originating from the meteorite as the target rocks are essentially sulphide-free [23].



**Figure 1.** The weathered Monturaqui impactite used in this study, similar to the material described in [23].

## 2.2. X-ray and Neutron Computed Tomography (CT)

The combination of neutron and X-ray computed tomography is used as a non-destructive method of studying the structural details and the composition of the impactites.

When a heterogeneous sample is irradiated by X-rays or neutrons, the incident beam is attenuated according to the attenuation properties and the thickness of the materials it transverses [11]. For a mono-energetic beam and a sample containing  $i$  (homogenous) materials, the attenuation follows the Beer-Lambert law:

$$I = I_0 e^{-\sum \mu_i d_i}, \quad (1)$$

where  $I$  is the transmitted intensity,  $I_0$  is the intensity of the incident beam,  $\mu_i$  (cm<sup>-1</sup>) is the linear attenuation coefficient of every material  $i$  being traversed, and  $d_i$  (cm) is the thickness, i.e., the path length of the radiation through material  $i$ . The linear attenuation coefficient  $\mu_i$  is a material-specific quantity and is proportional to its density:

$$\mu_i = \frac{\rho_i N_A}{M_i} \sigma_i, \quad (2)$$

where  $\rho_i$  is the mass density (g/cm<sup>3</sup>),  $N_A$  is the Avogadro constant ( $6.022 \times 10^{23}$  mol<sup>-2</sup>),  $M_i$  is the atomic mass (g), and  $\sigma_i$  is the total cross-section ( $10^{-24}$  cm<sup>2</sup>) of the material  $i$  and accounts for absorption and scattering. For X-rays  $\sigma_i$  includes the effects of photoelectric attenuation and incoherent Compton scattering (and coherent Rayleigh scattering), while for neutrons  $\sigma_i$  includes absorption and coherent and incoherent scattering. For both X-rays and neutrons,  $\sigma_i$  depends on the energy of the radiation and on the atomic number  $Z$ .

For silica-dominated geological samples measured using standard X-ray laboratory sources, the dominant attenuation process of X-rays below 50–60 keV is photoelectric absorption ( $\propto Z^{4-5}$ ) [32,33], whereas at higher energy Compton scattering predominates ( $\propto Z$ , or to first order  $\propto \rho$ ). This means that low-energy X-rays are more sensitive to differences in composition (e.g., for materials with similar mass density) than high-energy X-rays [34]. However, the former are also more easily attenuated, limiting the thickness of high-density material that can be penetrated.

Neutrons, having no charge, interact directly with atomic nuclei and can therefore travel deep into matter [11]; they can either be scattered in billiard-ball-like collisions or absorbed, changing the target

atom into a different isotope. The most important processes for cold and thermal neutrons are nuclear absorption and elastic scattering [11]. Interaction with high-energy neutrons will not be considered further here as it is less well suited to this specific case study. The neutron attenuation coefficients have no systematic relation to the atomic number of the material of interaction; neighbouring elements in the periodic system or even isotopes of the same element can exhibit large differences in neutron attenuation [11]. This irregular behaviour can help achieve contrast where X-rays provide similar absorption properties.

The principle of computed tomography, for both X-rays and neutrons, is that by measuring the attenuation of radiation traversing a sample at different angles, it is possible to compute volumetric data, in which an attenuation coefficient is calculated and assigned for every point in the volume. Projections are recorded over  $360^\circ$  by flat 2D CCD based detectors coupled with a scintillator material which converts the transmitted radiation into visible light. The most common volume reconstruction algorithms are independent of the radiation used and are well documented [35–37].

X-ray CT was carried out at the 3D Imaging Centre, DTU Lyngby (DK), using a Nikon XT H 225 scanner with tungsten target and applying an acceleration voltage of 200 kVp (479  $\mu$ A current). White beam neutron tomography was carried out at the IMAGINE beamline [38], the cold neutron imaging facility at the Laboratoire Léon Brillouin CEA/CNRS (FR). The respective values for the instrumental set-ups are reported in Table 1. Although meteoritic iron contains cobalt as a major element, the neutron investigation caused no significant activation of the sample, and the radiation intensity fell below the safety thresholds in about 1 week. In fact, the naturally occurring Co isotope,  $^{59}\text{Co}$ , is characterised by a very high neutron absorption cross section  $\sigma_{\text{abs}}$  ( $\sigma_{\text{abs}} \approx 82.7$  barns for neutrons of 4 Å); by neutron capture  $^{59}\text{Co}$  transforms into radioactive  $^{60}\text{Co}$ , which decays to  $^{60}\text{Ni}$  with a half-life of  $T_{1/2} = 5.2714$  years.

X-ray CT volume reconstruction was performed using the X-TEK 3D CT Pro developed by Nikon Metrology, while neutron projections were processed using the Octopus software package [39]. The reconstruction method is based on the filtered back-projection algorithm [40], considering cone-beam and parallel-beam geometry for X-ray and neutron tomography, respectively. The stacks of images obtained represent three-dimensional arrays of the linear attenuation coefficients for X-rays and neutrons. During reconstruction, the X-ray attenuation coefficients were rescaled using a linear transformation so as to correspond to mass density values, similar to the Hounsfield units commonly used in medical imaging. This calibration was possible because above 60 keV we assume that X-rays interact only by Compton scattering, which depends on electron density  $N_e$  ( $N_e$  is roughly  $\propto Z$ ). Having scaled to mass density values it is possible to identify the lithic phases and compare the attenuation coefficients to their theoretical density values. The applied scaling was verified using the iron rod sample holder, giving a mean X-rays attenuation value of  $7.9 \pm 0.8 \text{ g/cm}^3$ , compared with the iron density of  $7.87 \text{ g/cm}^3$ . The relatively large error is partly the result of noisy projections due to scattering and the use of a polychromatic source. The same scaling procedure could not be applied to the neutron data as there is no proportionality between the neutron attenuation coefficients and the atomic number of the materials.

X-ray laboratory sources, and polychromatic neutron imaging instruments, produce beams with a continuous energy spectrum. Energy-dependent attenuations mean less energetic X-rays are more likely attenuated, or even fully absorbed, when traveling through dense materials, producing so-called beam hardening (BH) effects. These were reduced by using an aluminium filter during acquisition and by applying a BH correction pre-set provided by the reconstruction software (X-TEK 3D CT Pro).

**Table 1.** Instrumental parameters set-ups for X-ray and neutron measurements.

Imaging Set-up	X-ray	Neutron
Pixel size ( $\mu\text{m}$ )	33.1	75.0
Projections ( $n^\circ$ )	3143	360
Magnification	1.32	1
CCD size (pixels)	$2048 \times 2048$	$2560 \times 2160$
Field of view (mm)	$150 \times 150$	$100 \times 100$
Source spectrum	200 kVp (479 $\mu\text{A}$ current)	cold neutrons (peaked at $\sim 4 \text{ \AA}$ )
Filter	Al, 0.250 mm thick	none
Rotating angle ( $^\circ$ )	0–360	0–360

### 2.3. Image Processing

X-ray CT contrast between high and low Z-dominated materials provided detail on the morphology of the impactite. This data-set was used to define vesicles and metallic spherules and perform a size variability analysis of these objects. Neutron imaging provided complementary attenuation information of the material matrix and inclusions. The combination of the two data-sets was used for the material segmentation, which was performed in Matlab.

#### 2.3.1. Image Registration

When a single imaging method cannot provide sufficient contrast to resolve the composition of the imaged object from its histogram, it is possible to take advantage of the spatial correlations of the intensity distributions from multiple registered data-sets under different modalities. Plotting the attenuation coefficients given by the two modalities in a bivariate histogram may aid in the separation of phases with distinct compositions, forming ‘clusters’ of intensity within the bivariate histogram plot.

To achieve this, we have manually pre-aligned the two data sets (through rotations and reslice functions) in FIJI [41] and registered them (scaled and aligned on a common coordinate system) in the Statistical Parametric Mapping SPM8 software package [42] using a rigid transform and the normalised mutual information similarity metric [43,44]. Rigid body registration only allows for rotations and translations, and therefore does not deform the objects. Normalised mutual information is one of the most common image similarity metrics for multi-modal registration [45]. The X-ray data set was used as fixed volume (Reference Image) to which the neutron volume (Float Image) was co-registered. An example slice from the two datasets is shown in Figure 2, before and after the registration transformation. While the transformation applied to the Float Image does not deform the object, the difference in the appearance of the slices from the Float and the Co-Registered images is due to the fact that the transformation is applied in 3D.

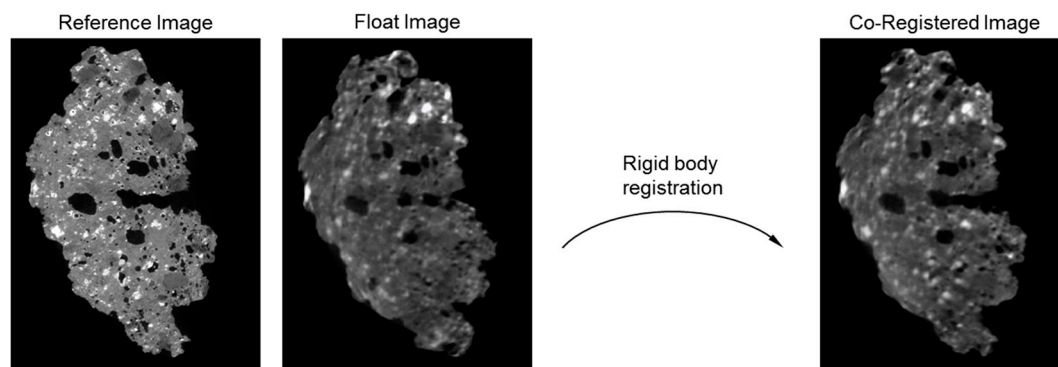


**Figure 2.** Example of X-ray (Reference Image) and neutron slices before (Float Image) and after (Co-Registered Image) rigid body registration of the 3D volumes.

Because of the higher resolution achieved in the X-ray scan (see Table 1), the neutron volume (float image) was up-sampled in order to match the voxel dimensions of the X-ray volume (reference image). Although this process may introduce errors (e.g., in the material segmentation), it preserves the morphological details of the sample. The resulting volume dimensions are  $1072 \times 1610 \times 1061$  voxels of  $33.1 \mu\text{m}$  size, for a total volume of  $3.54 \times 5.33 \times 3.51 \text{ cm}^3$ . The registration process allowed for voxel-wise comparison between the two data sets.

In addition, in order to simultaneously visualise both attenuation coefficients, we converted the grey scale values by merging them into false colour images, using JET and RGB colour models.

### 2.3.2. Materials Segmentation

Image segmentation was performed by classifying the voxels in different material classes depending on their bi-modal grey scale values. In order to focus the segmentation on the impactite only, we used the X-ray volume (see Figure 3a) to exclude air and vesicles by grouping them into the background. In doing so, all vesicles smaller than the achieved resolution contribute to a density reduction of the material in consideration. The background mask thus created was used to estimate porosity in the object (see Section 3.3.1).

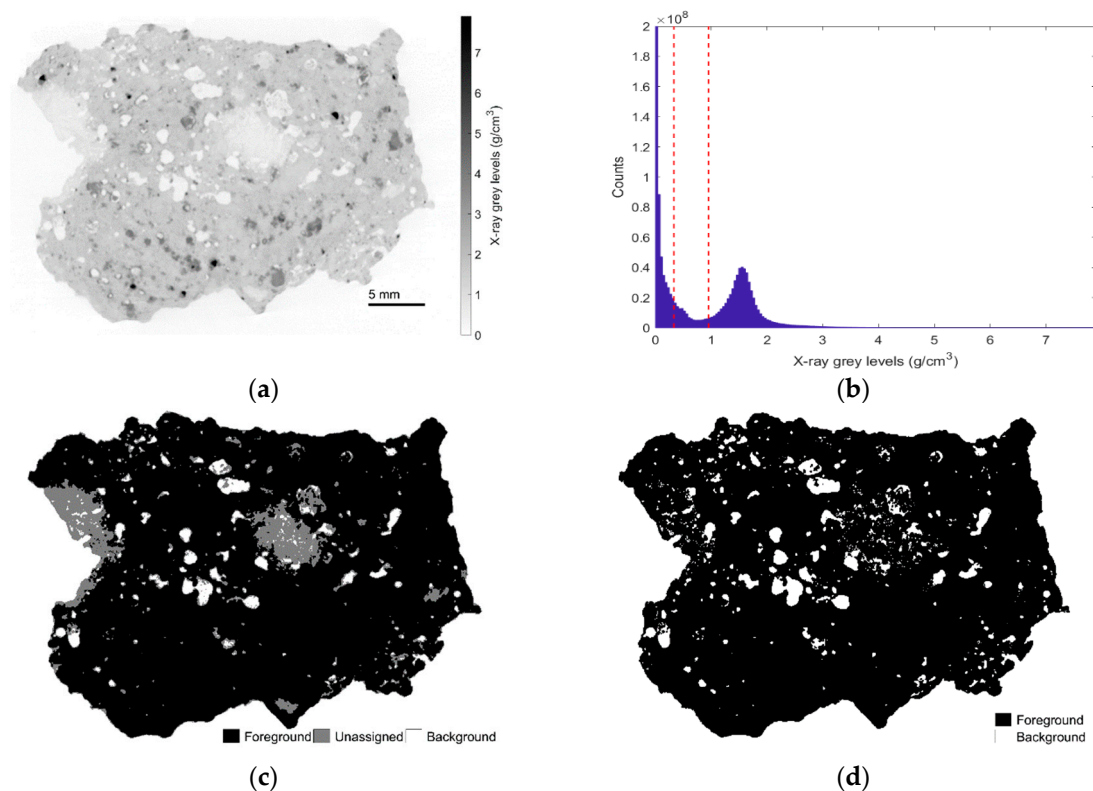


**Figure 3.** (a) Corresponding slices ( $z = 673$ ) from X-ray volume used as a starting point for the impactite mask creation; (b) Histogram of the X-ray volume with the two thresholds used for segmenting the solid material (foreground) from air (background); (c) Dual intensity thresholding model with background in white, low-density material and edges (unassigned voxels) in grey, and foreground object (representing the voxels above the second threshold) in black; (d) Final mask in black selecting impactite (foreground). X-ray attenuation values above 7.9 have been truncated for visualization purposes.

X-ray imaging for lithic samples generally provides a high contrast between an object and voids. However, the occurrence of voxels, representing highly-vesiculated silicate-dominated volumes of materials with a low average density (see light grey areas in Figure 3a showing the negative of the attenuation, where white corresponds to no attenuation and black to high attenuation), did not allow

the use of a simple threshold. The low-density, highly-vesiculated phase is in fact characterised by the same greyscale values of some of the edge voxels (gradient between the object and the empty pores) and inner vesicles.

The impactite mask was created through dual intensity thresholding (see Figure 3b), with thresholding values computed by minimising the intraclass variance [46]. Figure 3c shows, in white, the voxels below the first threshold representing the air (background), in black, the foreground object representing the voxels above the second threshold, and in grey the unassigned voxels with values in between. The unassigned voxels were treated separately by applying morphological transformations to enhance the image contrast (top-hat filter), which acted like a high-pass filter to extract the bright areas of the image. This approach allowed us to assign inner vesicles and edge voxels to the background representing air, while keeping the low-density phases in the foreground object. The resulting mask is shown in Figure 3d, where the impactite is visualised in black and the air is represented in white.

As the impactite is dominated by silicate-rich glasses, most of its voxels lie within a narrow neutron and X-ray attenuation range. Minor phases could be identified by the presence of clusters that can be visualised as local maxima by plotting the voxel counts in a logarithmic scale, as shown below in Figure 4.

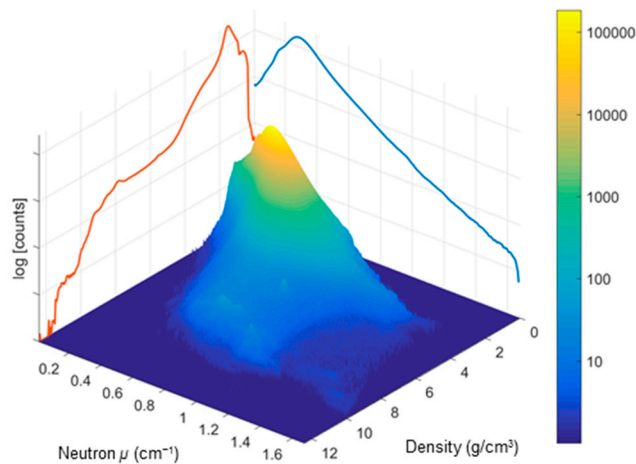


**Figure 4.** Bi-modal histogram of neutron attenuation coefficient  $\mu$  versus density, with voxel counts per bin in logarithmic scale: the plot is compared to the respective X-ray (orange) and neutron (blue) histograms. Only impactite voxels selected through the aforementioned mask are shown (see Section 2.3.2).

Intensity-based segmentations are very effective when the object is constituted by few materials with well separated peaks in the bivariate histogram. However, overlap in distributions may lead to noisy segmentation. The noise can be alleviated by considering contextual information, utilizing the fact that short-range regions are often homogeneous. In the present analysis we performed a Markov random field (MRF) segmentation [47], a probabilistic model that takes into account the likelihood of assigning each voxel to a specific label, not only depending on its grey scale value, but also on the label assigned to the neighbouring voxels.

### 2.3.3. Morphology

Following segmentation, a binary mask was defined for the metallic spherules (designated class 8, see Table 2 for defining parameters) and another for the vesicles derived from the background mask described above (see white area represented in Figure 3d). Using the two binary masks we performed a connected components analysis to evaluate the distribution and size variability of the metallic spherules and vesicles. Connected components analysis is used to label voxels pertaining to



the same object (or region of space), as defined by the mask. Due to the achieved spatial resolution, we only considered objects larger than 2 voxels ( $\approx 7.2 \times 10^4 \mu\text{m}^3$ ). In order to calculate the size of the objects, we analysed the connected components of the two masks considering a 3D neighbourhood of 6 voxels. Since these objects are far from perfect spheres, especially the larger ones, we estimated their volume simply by the number of constituent voxels.

### 3. Results

#### 3.1. Visualisation

Impactite X-ray and neutron volumes are plotted in a bivariate histogram (see Figure 4) showing voxel-wise comparison of the attenuation values between the two modalities. This plot aids in the identification phases of defined composition. This in turn can help us consider the heterogeneity of the sample.

Corresponding slices from the registered X-ray and neutron tomography volumes are shown in Figure 5 for direct comparison, together with the voxel-to-voxel correspondence plotted in a bi-modal histogram. For a better visualization of the slices we use a colour scheme where high intensity (in bright) correspond to low attenuation. X-ray imaging provides high contrast for the metallic spherules (in black), while neutrons highlights both the spherules (mainly due to Fe, Ni and Co) and their hydrogen-containing oxidic corrosion products (mainly due to the presence of hydrogen).

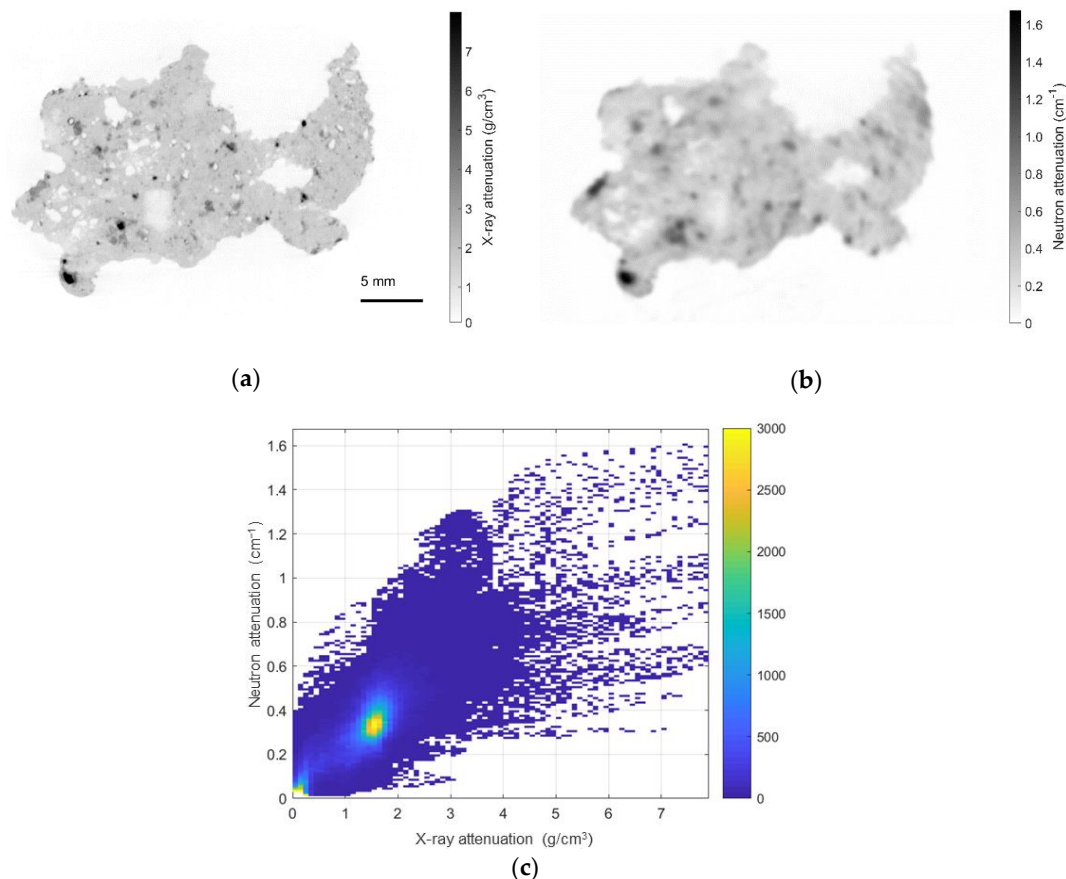


**Figure 5.** Corresponding slices ( $z = 913$ ) from a reconstructed volume of the Monteraqui impactite using (a) X-ray and (b) neutrons. High intensity (bright) correspond to low attenuation coefficients. The areas of lowest absorption correspond to voids in the impactite; (c) Bi-modal histogram relative to the selected slice. X-ray attenuation values above  $7.9 \text{ g/cm}^3$  have been truncated for visualization purposes.



False colour images are an effective way of simultaneously visualizing images from multiple modalities; some of the possible combinations obtained using JET and RGB colour models are shown in Figure 6, alongside the respective colour map. These colour schemes provided the best combination for this particular dataset. The false colour images were used to visually identify features of interest in the impactite, such as corrosion areas (highly attenuating for neutrons but not for X-rays) surrounding some of the Fe-Ni spherules (high attenuation in both datasets). All X-ray attenuation values above 7.9 have been truncated for visualization purposes.

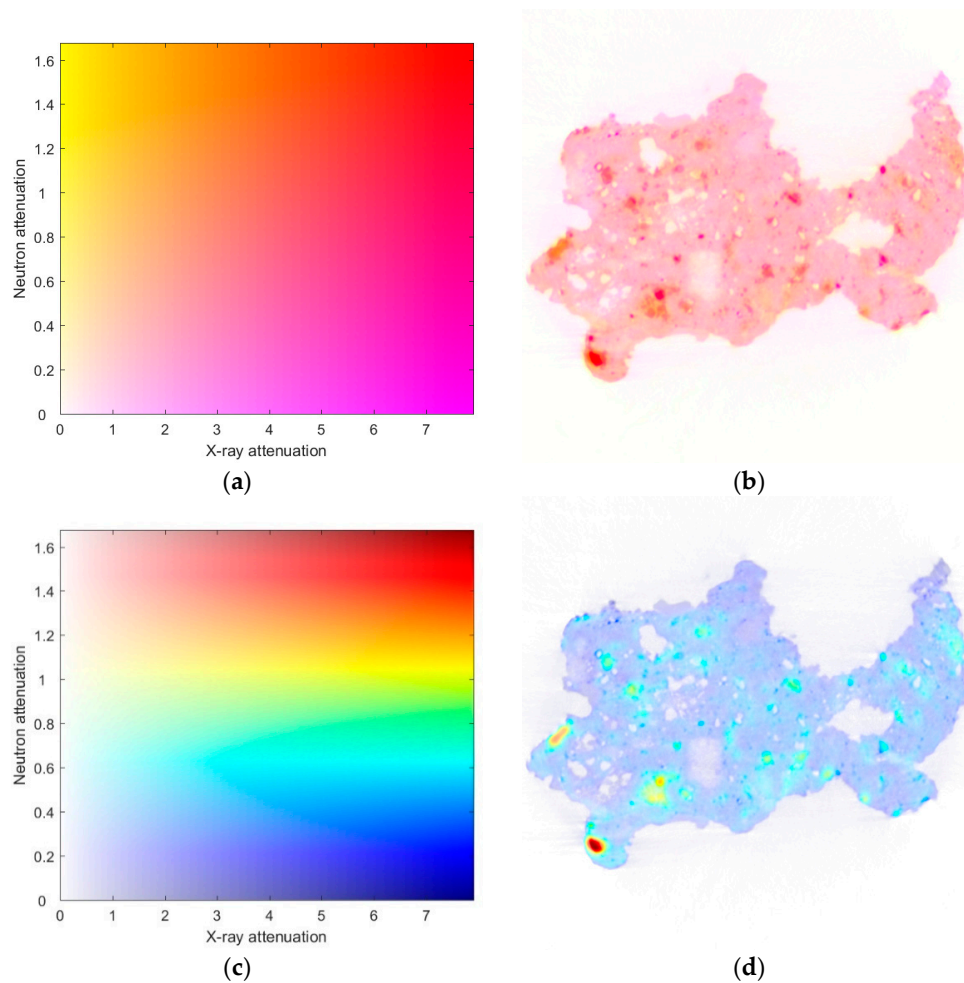


**Figure 6.** (a) RGB colourmap and (b) corresponding RGB false colour representation of slice  $z = 913$ ; (c) JET colourmap and (d) corresponding JET false colour representation of slice  $z = 913$ .

### 3.2. Materials Segmentation

Considering the expected mineralogical composition (based on literature, see Section 2.1) of the impactite and the clustering of the voxels as plotted in the bivariate histograms in Figures 4 and 5c, we grouped the minerals in 8 materials classes, according to which we performed the segmentation. Table A1 in the Appendix A reports the mean attenuation values for each class used as starting values for the MRF segmentation.

The X-ray and neutron attenuation ranges that the material classes cover are visualised in Figure 7. Comparisons to the theoretical density and neutron linear attenuation values of some of the expected minerals are reported Table 2. As porosity contributes to density reduction, the theoretical density and neutron attenuation of most phases are higher than the experimental ones. Because of the multiple

and complex mineralogy of the lithic fragments, we did not calculate their theoretical density  $\rho$  and neutron linear attenuation values  $\mu$ .

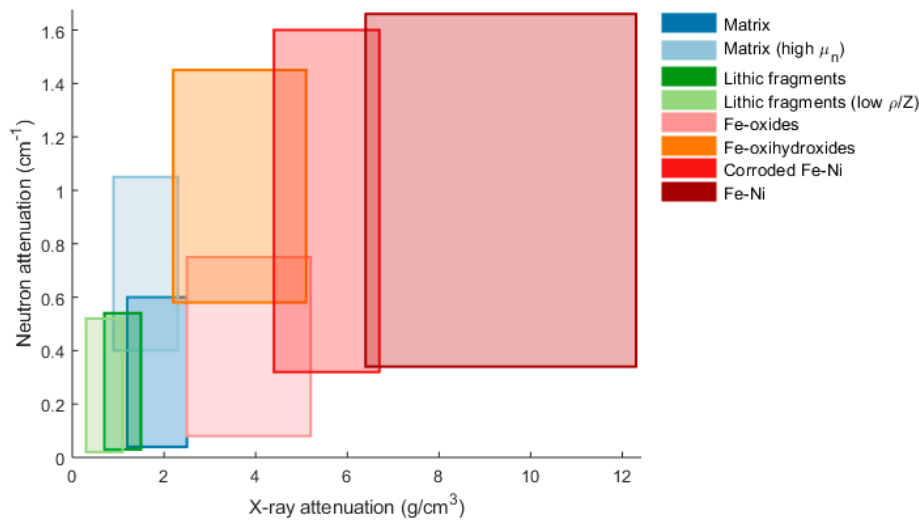


**Figure 7.** X-ray and neutron attenuation ranges for the different material classes identified in the impactite.

**Table 2.** Theoretical density  $\rho$  (g/cm<sup>3</sup>) and linear neutron attenuation  $\mu$  (cm<sup>−1</sup>, for 4 Å neutrons) values of selected minerals (non-porous) expected in the impactite [23] and corresponding segmentation material class and attenuation ranges.

Mineral	Chemical Formula	$\rho$ (g/cm <sup>3</sup> )	$\mu$ (4 Å) (cm <sup>−1</sup> )	Class Colour	Material Class	X-ray $\rho$ (g/cm <sup>3</sup> )	Neutron $\mu$ (cm <sup>−1</sup> )
Quartz	SiO <sub>2</sub>	2.65	0.293	■	Matrix glass	1.2–2.5	0.04–0.60
Magnetite	Fe <sub>3</sub> O <sub>4</sub>	5.17	0.926	■	Iron oxides	2.5–5.2	0.08–0.75
Hematite	Fe <sub>2</sub> O <sub>3</sub>	5.24	0.936	■	Iron oxides	2.5–5.2	0.08–0.75
Ilmenite	FeTiO <sub>3</sub>	4.79	0.898	■	Iron oxides	2.5–5.2	0.08–0.75
Goethite	FeO(OH)	4.13	3.038	■	Iron oxihydroxides	2.2–5.1	0.58–1.45
Troilite	FeS	4.61	0.616	■	Fe-Ni + troilite	4.4–6.7	0.32–1.60
Pyrrhotite	Fe <sub>(1-x)</sub> S	4.61	0.616	■	Fe-Ni + troilite	4.4–6.7	0.32–1.60
Kamacite	Fe <sub>0.9</sub> Ni <sub>0.1</sub>	7.9	1.576	■	Fe-Ni spherules	6.4–12.3	0.33–1.68
Taenite	Fe <sub>0.8</sub> Ni <sub>0.2</sub>	8.01	1.672	■	Fe-Ni spherules	6.4–12.3	0.33–1.68
Ferrite	Fe	7.89	1.469	■	Fe-Ni spherules	6.4–12.3	0.33–1.68

An example of the segmentation is shown in Figure 8, where individual X-ray and neutron slices are compared. Matrix glass materials are shown in blue, lithic inclusions in shades of green, oxidic corrosion products in orange/pink, and metallic phases in shades of red. In Table 3 the volume fraction of each material class is reported.

**Table 3.** Material classes and respective volume fraction of the solid volume of the impactite as resulted from the MRF segmentation.

#	Class Colour	Material	Volume %
1	■	Matrix glass	78.14
2	■	Matrix (high neutron attenuation $\mu_n$ )	0.83
3	■	Lithic fragments	13.78
4	■	Lithic fragments (low $\rho/Z$ )	2.90
5	■	Iron oxides (dominantly maghemite)	3.16
6	■	Iron oxihydroxides (dominantly goethite)	0.89
7	■	Fe-Ni corroded spherules or containing troilite	0.19
8	■	Fe-Ni spherules	0.12

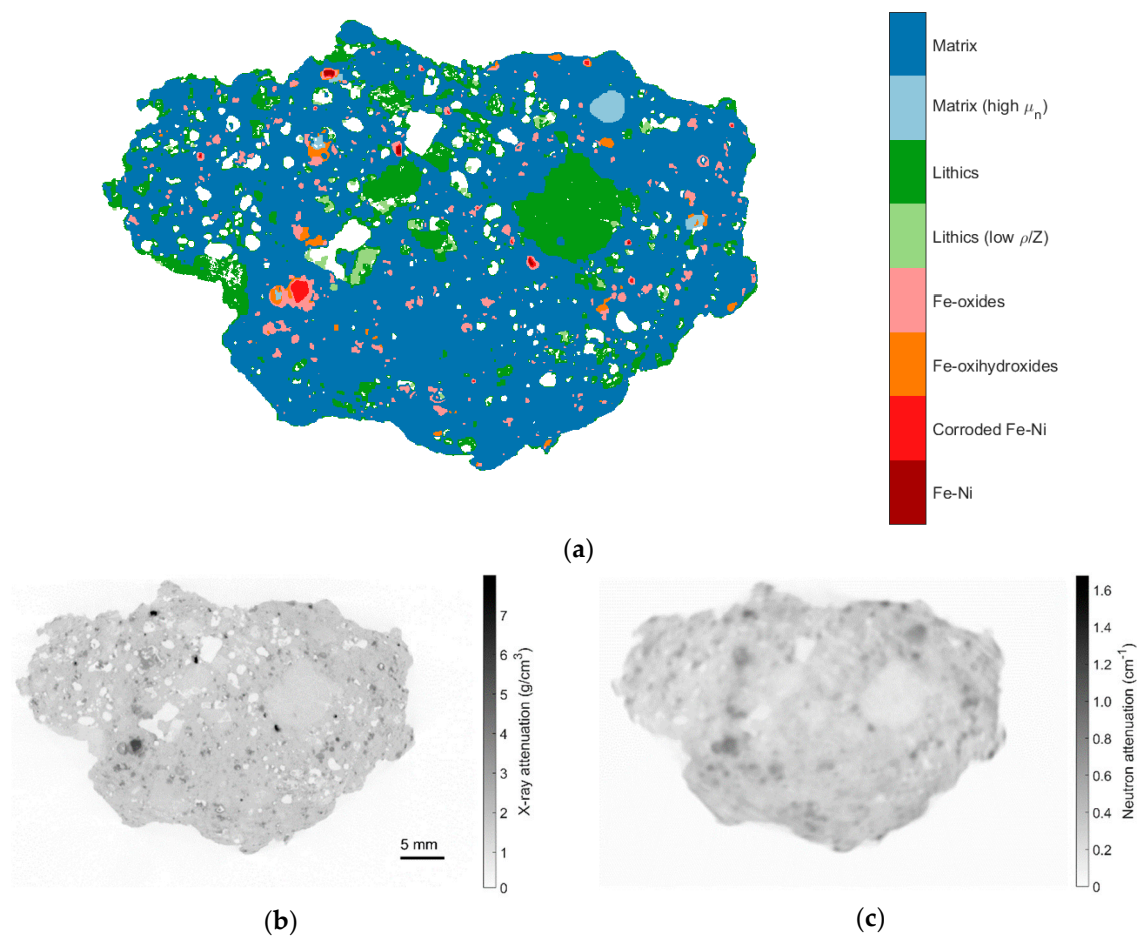


**Figure 8.** (a) Segmentation example with the 8 material classes compared to the corresponding (b) X-ray and (c) neutron slices ( $z = 415$ ).

### 3.3. Morphology

#### 3.3.1. Vesicles Analysis and Quantification

The connected components analysis detected 60,151 vesicles larger than 2 voxels, making up  $\approx 7.19\%$  of the total impactite volume. The majority of vesicles are relatively small (median value of 18 voxels, which corresponds to  $6.5 \times 10^{-4} \text{ mm}^3$ ), but the size distribution is very broad, ranging up to 8 M voxels (corresponding to a volume of  $0.29 \text{ cm}^3$ ). For this reason, we grouped the vesicles in five different ranges of increasing size. The classes densely cover the lower-end of the size distribution, with objects larger than 5000 voxels grouped in the last category. The inclusions that fill some vesicles are not accounted for in the volume quantification.

A 3D rendering of the thus-classified vesicles is reported in Figure 9, with colour representing the five different vesicle size ranges as subdivided according to the legend. As can be seen from the 3D rendering and the horizontal cut in Figure 9, vesicles larger than 5000 voxels (pale green) make up most of the volume, while smaller objects clearly dominate in number. This is more clearly represented by the bar plots in Figure 10. This confirms that, while small-scaled pores are more frequent (see Figure 10a), almost 80% of the volume of the impactite is grouped in vesicles constituted of more than 5000 voxels. From the section it appears that the vesicles are ubiquitous within the material, yet quite unevenly distributed and particularly rare within the lithic fragments.

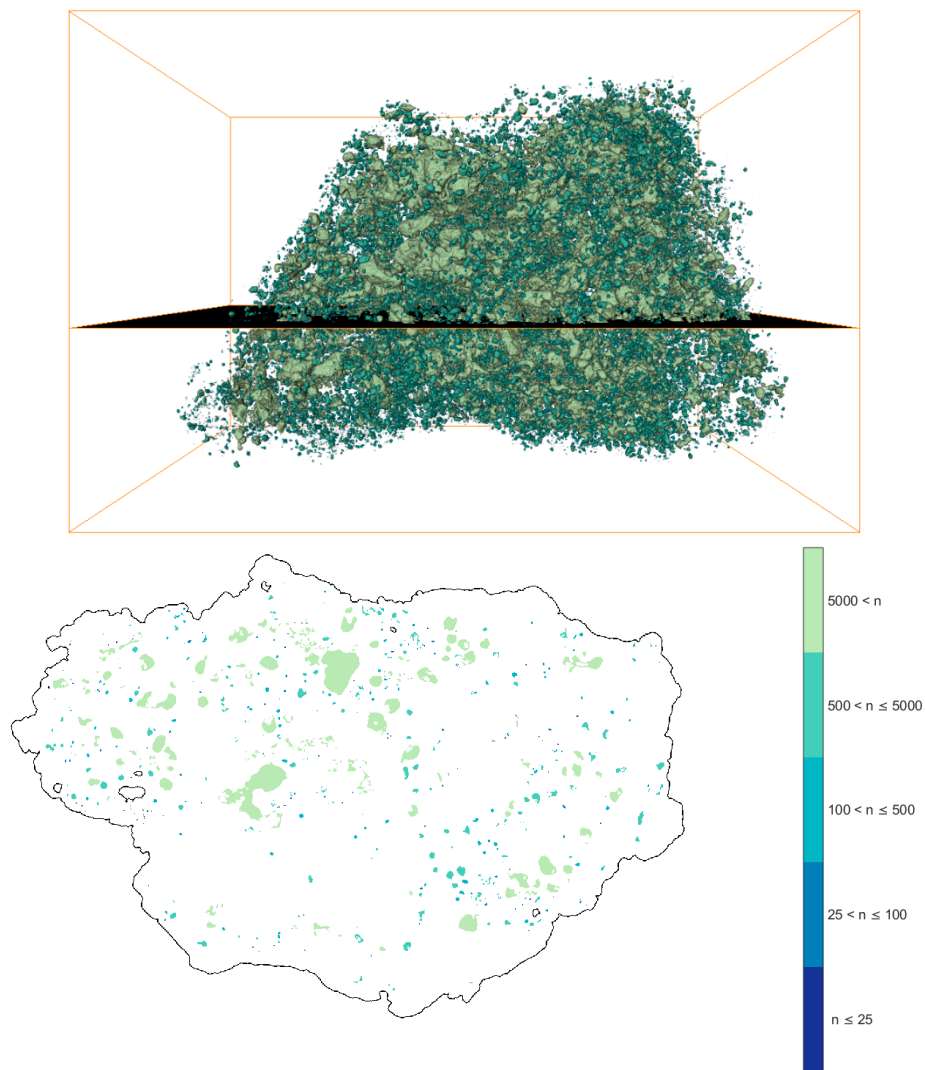


**Figure 9.** Example of vesicles distribution in the impactite: **(above)** 3D rendering of the dense pore structure created with Avizo software; **(below)** virtual cut (slice  $z = 415$ ), with colour representing the 5 different vesicle size ranges as subdivided according to the legend, with  $n$  the number of voxels per vesicle. In black is outlined the edge of the impactite. Note that black lines inside the sample edge represent porosity connected to the outside.

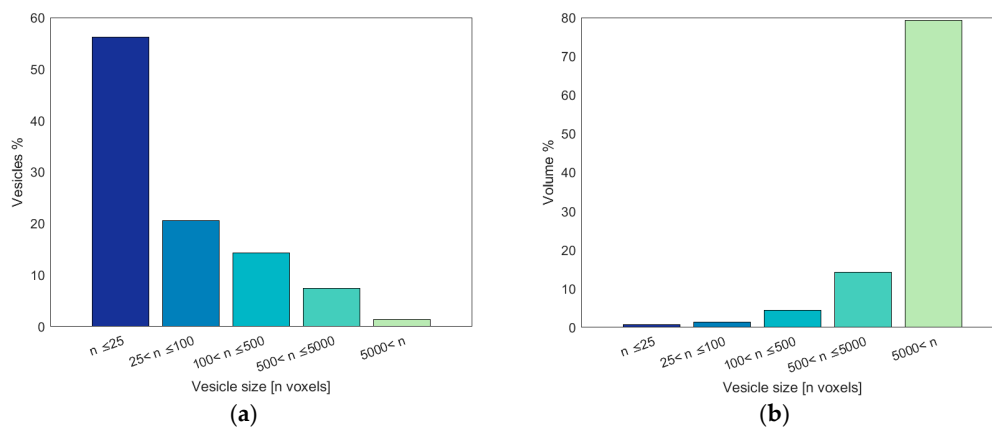


**Figure 10.** Quantification of vesicles analysis of Monturaqui impactite. **(a)** Vesicles size distribution and **(b)** total volume distribution per class.

### 3.3.2. Spherules Analysis and Quantification

The connected components analysis detected 1412 Fe-Ni metallic spherules (class 8 according to Table 2), representing  $\approx 0.12\%$  of the impactite solid volume. Volumes of corroded or partially corroded spherules (classes 5–7 according to Table 2) are not included in the analysis as corrosion causes volume expansion and the formation of porosity. The spherules have a median size of 118 voxels (which corresponds to  $4.3 \times 10^{-3} \text{ mm}^3$ ), with a size distribution ranging up to 27 k voxels (volume of  $9.7 \times 10^{-1} \text{ mm}^3$ ). Similarly, to the vesicle analysis, we grouped the spherules in 5 size ranges. Figure 11 shows the 3D rendering of the five spherule classes, with detail of a transversal slice. Size distribution and volume fraction per class of spherules are shown in Figure 12.

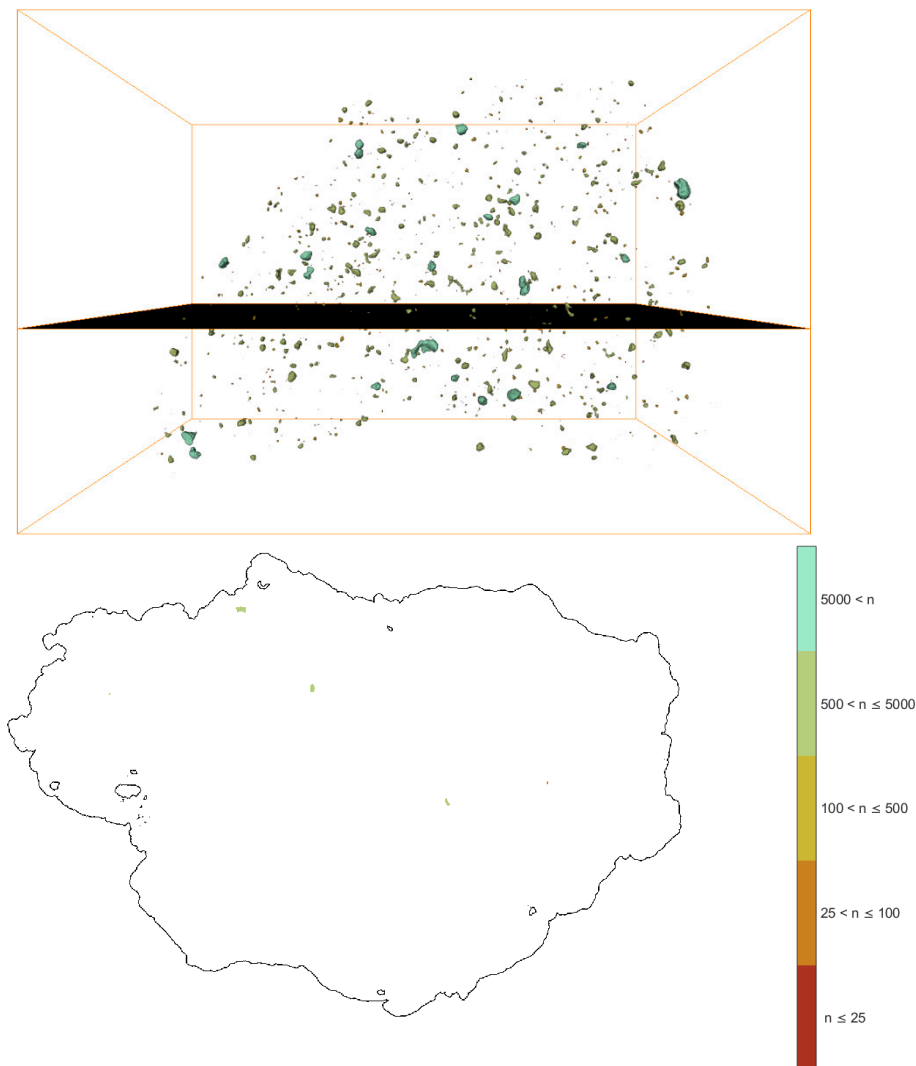


**Figure 11.** Example of spherules distribution in the impactite: **(above)** 3D rendering of the spherules; **(below)** virtual cut (slice  $z = 418$ ), with colour representing the 5 different size ranges as subdivided according to the legend, with  $n$  the number of voxels per spherule. In black is outlined the edge of the slice represented. Note that black lines inside the edge represent porosity connected to the outside.

Monturaqui spherules in some studies [23,30] showed a correlation between compositional variation in Fe-Ni and size, with spherules smaller than 0.1 mm in diameter more enriched in Ni (and therefore Co) than larger ones. A diameter of approximately 0.1 mm corresponds to spherules in the first size range, with a voxel number  $n \leq 25$ . This elemental variation, called fractionation, was attributed to partitioning and diffusion of Fe from the spherules into the surrounding impact

glass and to selective oxidation of Fe [15,48], causing the formation of a Ni-rich rim in the spherule surrounded by a Fe-rich halo (Fe >30%) in the silicate melt [30]. Although the available resolution was not sufficient to detect such detailed features, it was possible to distinguish such spherules by the different attenuation values depending on their size.

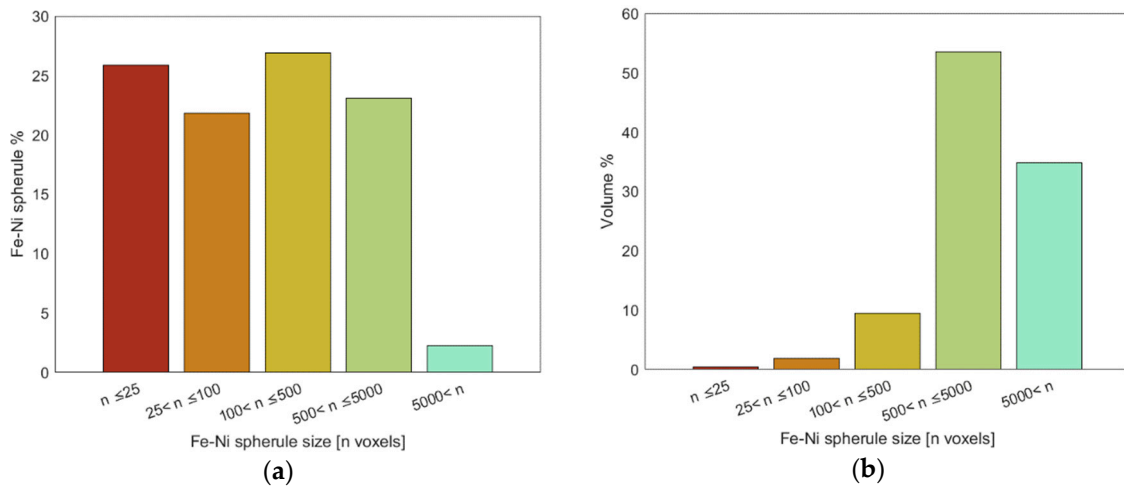


**Figure 12.** Quantification of spherule analysis of Monturaqui impactite. (a) Spherules size distribution and (b) total volume distribution per class, where  $n$  is the number of voxels (33.1  $\mu\text{m}$  size).

The mean X-ray and neutron attenuation values are plotted in Figure 13 for the five spherules size classes. This indicates an unexpected correlation between size and attenuation, with larger objects being more attenuating for both X-rays and neutrons. The presence of a higher amount of Ni in smaller spheres would in fact increase their density and neutron attenuation coefficient (see values for taenite, kamacite and ferrite in Table 2). Clarification of this contradiction will require a focussed future destructive analyses guided by the imaging data.

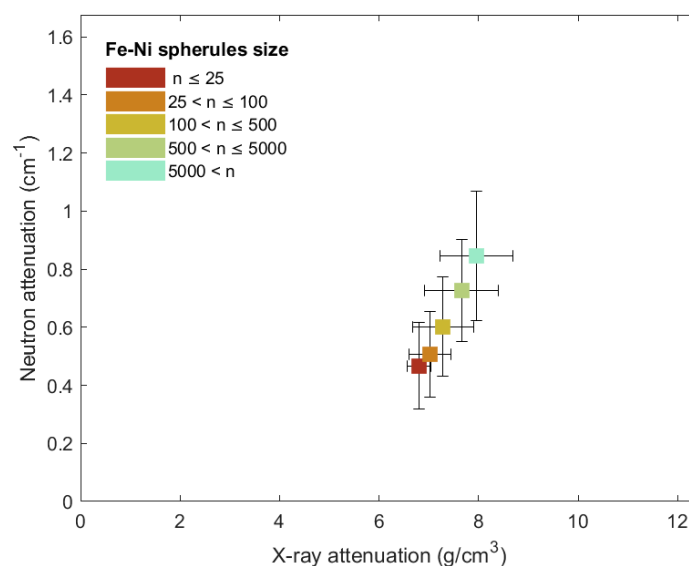


**Figure 13.** Mean X-ray and neutron attenuation values and standard error for the five spherules size classes, where  $n$  is the number of voxels (33.1  $\mu\text{m}$  size).



### 3.3.3. Morphological Details

Lithic fragments (see Figure 14) constitute common inclusions ( $\approx 16\%$  in volume) in the matrix and have a heterogeneous genesis and composition. Further detailed inspection of the volume data enabled us to identify otherwise hidden morphological features, such as the presence of shocked and unshocked lithic fragments, layers of corrosion covering some of the vesicles, and evaporites (see Figure 15d,e).

Evaporites are mineral aggregates formed by the evaporation of water. They appear as partial and similarly oriented infilling of some of the larger vesicles by angular salt crystals (see green framed inserts in Figure 15). These precipitation salts have escaped unnoticed in past studies, possibly because the salts were removed during sample preparations. Layers of oxidic corrosion products covering inner vesicles (see red framed inserts in Figure 15) are also a result of the presence of water (weathering) and are most likely due to the alteration of metallic spherules associated with the surface of some vesicles. This hypothesis is corroborated by the presence of corroded iron spherules in some pores showing this alteration layer (see Figure 15b). This finding indicates that, although water overall is scarce, it makes a significant and lasting imprint on a local scale.

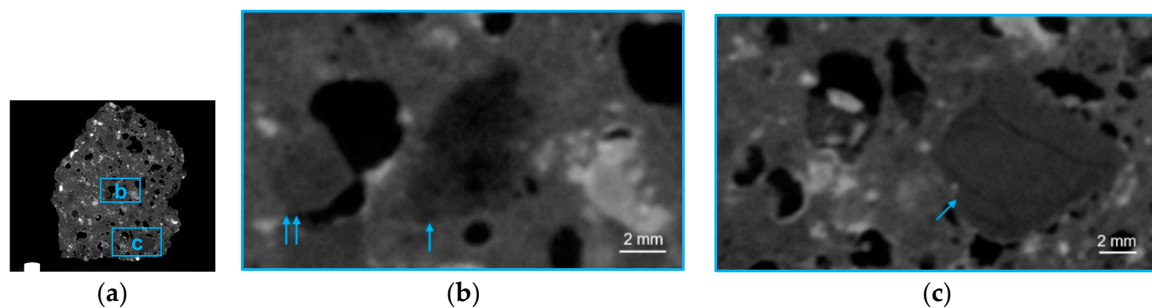


**Figure 14.** (a) Slice of the X-ray volume of the impactite showing inclusions of lithic fragments; (b) detail of the central part of the impactite showing a highly vesiculated fragment (↑), next to an unshocked fragment (↑↑); (c) close-up of a shocked lithic fragment.

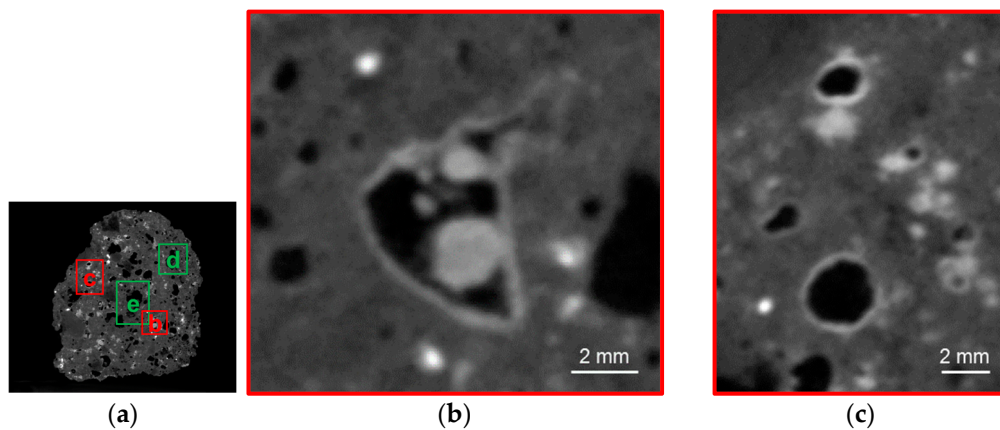


**Figure 15.** Cont.

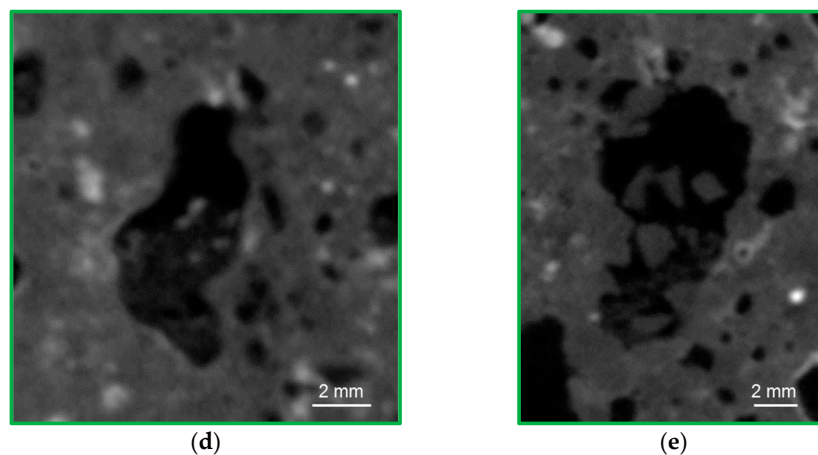


**Figure 15.** (a) Slice of the X-ray volume of the impactite where the green frames highlight the presence of evaporites and in the red frames show corrosion layers covering inner vesicles; (b) detail of a large vesicle covered by the corrosion layer and the residua of corroded iron spherules; (c) close-up detail of two large and three small vesicles covered by the corrosion layer; (d) close-up detail of the top-right evaporite; (e) close-up detail of the evaporite filling the large central vesicle.

#### 4. Discussion and Conclusions

X-ray and neutron tomography are applied in a bi-modal approach for an exemplary 3D characterisation of a Monturaqui impactite. The different interactions of X-rays and neutrons with matter allowed us to exploit the complementary information of both modalities.

The two separate data sets have been registered successfully and allowed for the identification of a rich variety of phases in the sample in accordance with the literature. False colour visualisation approaches proved their efficiency for visualisation and inspection of the bi-modal volume data.

MRF segmentation of the volume, using attenuation information from both modalities, allowed the identification and separation in particular of materials which showed similar attenuation levels in single modalities. The efficiency of the bi-modal approach is demonstrated e.g., in the distinction between oxide and oxyhydroxides, and the detection of a low-density phase in the matrix characterised by high neutron attenuation.

Most of the object is found to be composed of low-density phases with overlapping attenuation distributions. Yet some classification uncertainty remains as materials listed as general “silica matrix” and “lithic fragments” could not be further classified. Despite the complementary radiation utilized, sub-resolution porosity cannot be analysed. Identical grey levels could either be associated with differences in porosity or differences in composition, but this cannot be distinguished by the bi-modal data.

The metallic content was quantified as 0.12% of the volume, distributed among 1412 spherules—a much lower amount than reported in the literature ( $\sim 4.6\%$ ) [30]. This could be partly due to the fact that we excluded the partially corroded particles and the related corrosion products as they generally involve volume expansion. By including these, the total metal phases accounts for 4.36% of the volume, in line with values from the literature [30].

Analyses resulted in detailed data on the morphology of the impactite, and on the distribution and size variability of vesicles. We identified 60,151 vesicles, constituting  $\approx 7.2\%$  of the total impactite volume. The porosity size range is very large, and small sized structures (below 25 voxels,  $9.07 \times 10^{-4} \text{ mm}^3$ ) are dominant in number, but not in volume.

In comparison to previous investigations using polished sections [23], the numbers of different types of objects identified (e.g., 60,151 vesicles and 1412 metal spherules) are orders of magnitudes higher, increasing the trustworthiness of trends in the data.

Hydrogen containing phases, such as iron corrosion products from the weathering of metallic spherules, could be clearly identified. However, extensive alteration of the metallic parts (and therefore the high, incoherent scattering due to hydrogen) hindered the identification of variations of trace elements such as Cu, Re, Ir, Pt, Au, and Co, which in principle provide high contrast in neutron imaging. These trace elements may be better detected in non-altered (hydrogen-free) impactite samples.

Contrary to results reported in past studies [23,30], the attempted identification of kamacite (5–10% Ni) and taenite (20–74% Ni) appeared to reveal that larger spherules are characterised by a higher Ni content. This could be due to Ni-rich spherules being more resistant to corrosion and therefore remaining larger. Alternatively, the results might be biased by image artefacts due to the depletion of radiation across larger particles, especially in the case of X-rays—though less for neutrons. Clarification of this discrepancy might require a focussed destructive investigation guided by the presented data.

Rare, micron sized precipitation of salt crystals in miniaturized structures akin to evaporites have been detected. These weathering products have escaped unnoticed in previous studies, possibly because the salts were removed during sample preparations.

We conclude that bi-modal imaging can provide a wealth of information on multi-phase objects, such as impactites, non-destructively and is hence highly suited in particular for initial studies which preserve the specimen for further potentially destructive studies, if still required. The rich imaging data can also guide further studies in order to keep destruction to a minimum and maximise focussed information extraction. A wide range of exemplary analytical and visualisation tools have been demonstrated successfully for use in such volumetric studies.

**Author Contributions:** C.B.K., A.B.D. and M.S. conceived and supervised the project; A.F., M.S., F.O. and C.G. acquired the imaging data; A.F. performed tomography reconstruction, volume registration (with contribution from K.M. and M.L.), data analysis, and created figures; V.A.D. wrote the segmentation algorithm and helped improving figures; A.F. wrote the original manuscript and curated review and editing with inputs from the other authors.

**Acknowledgments:** Camilla H. Trinderup and Knut Conradsen from the Technical University of Denmark are gratefully acknowledged for the useful discussion. The authors wish to thank V.F. Buchwald for providing the sample. The 3D Imaging Centre at the Technical University of Denmark is also gratefully acknowledged. This project receives funding from the European Union's Horizon 2020 research and innovation programme under grant agreement No. 654000. This work has been partially financed by the Interreg project "ESS & MAX IV: Cross Border Science and Society". Constructive comments from the reviewers helped to significantly improve the manuscript.

**Conflicts of Interest:** The authors declare no conflict of interest. The founding sponsors had no role in the design of the study; in the collection, analyses, or interpretation of data; in the writing of the manuscript, and in the decision to publish the results.

## Appendix A

Slice  $z = 415$ .

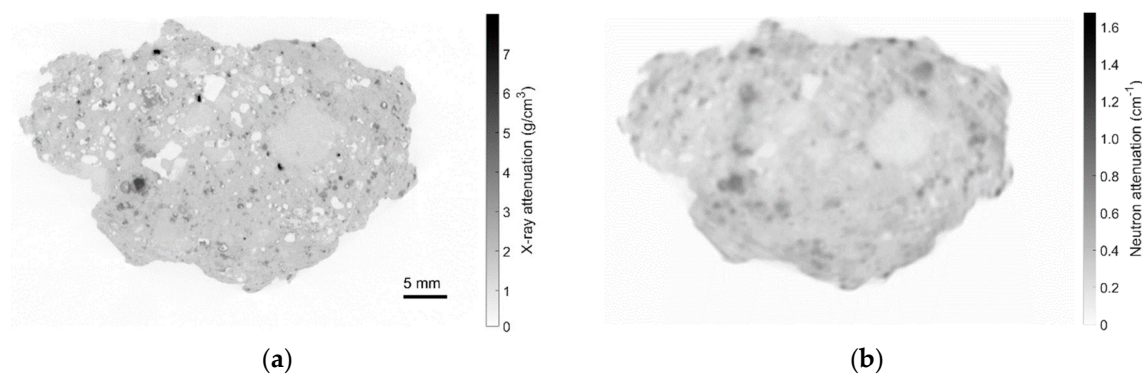
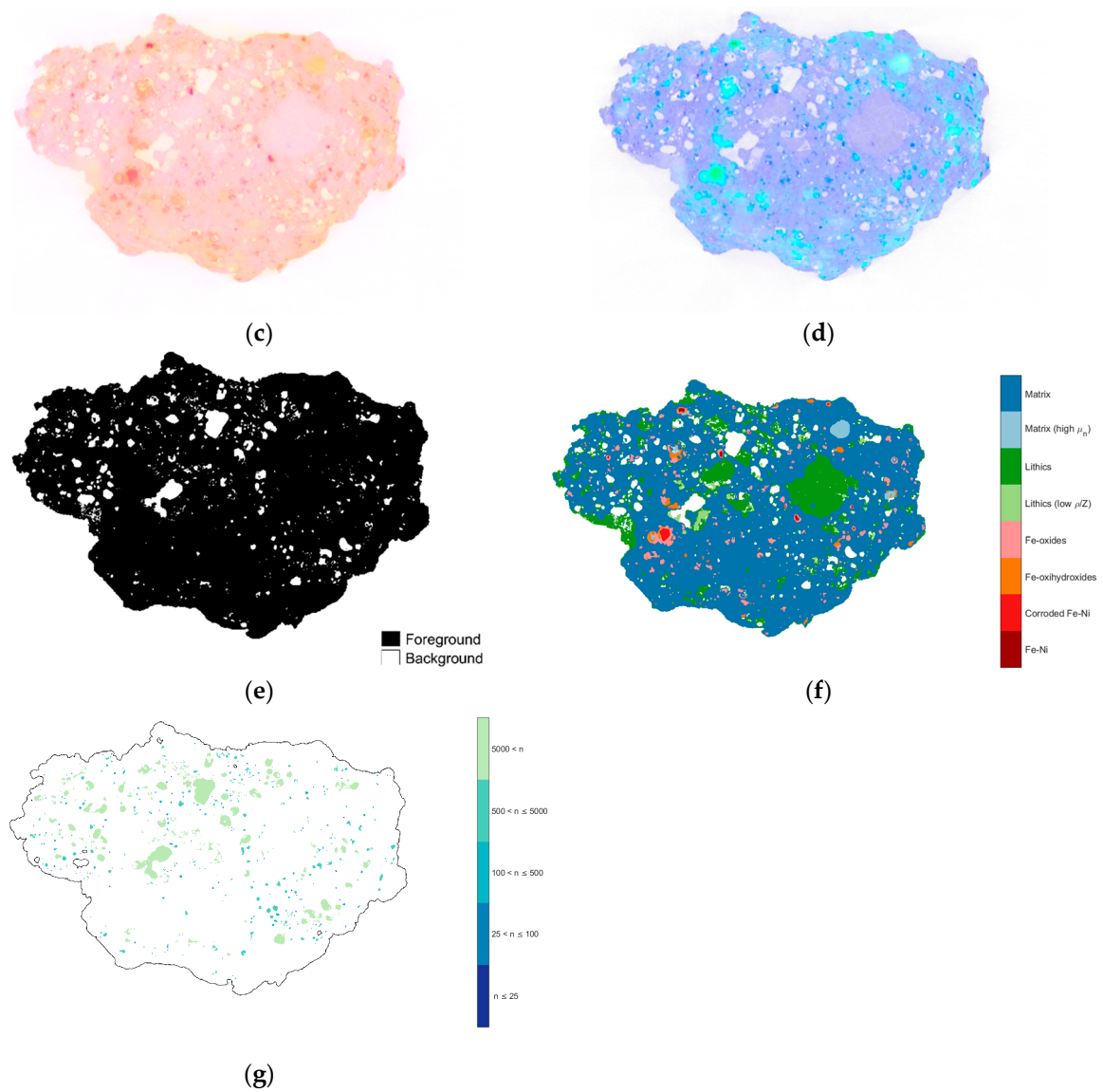
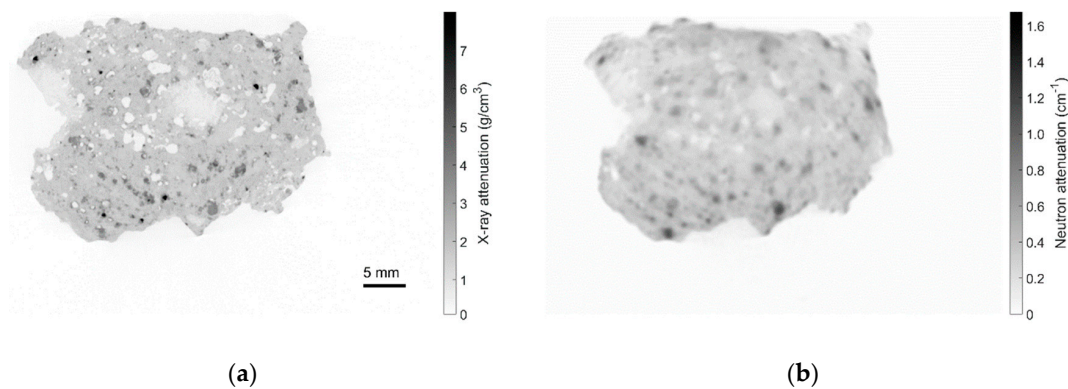


Figure A1. Cont.



**Figure A1.** Impactite corresponding slices for  $z = 415$ . (a) X-ray volume; (b) neutron volume; (c) RGB false colour representation; (d) JET false colour representation; (e) mask selecting the impactite (foreground); (f) MRF segmentation; (g) vesicle distribution of the impactite.

Slice  $z = 673$ .



**Figure A2.** Cont.



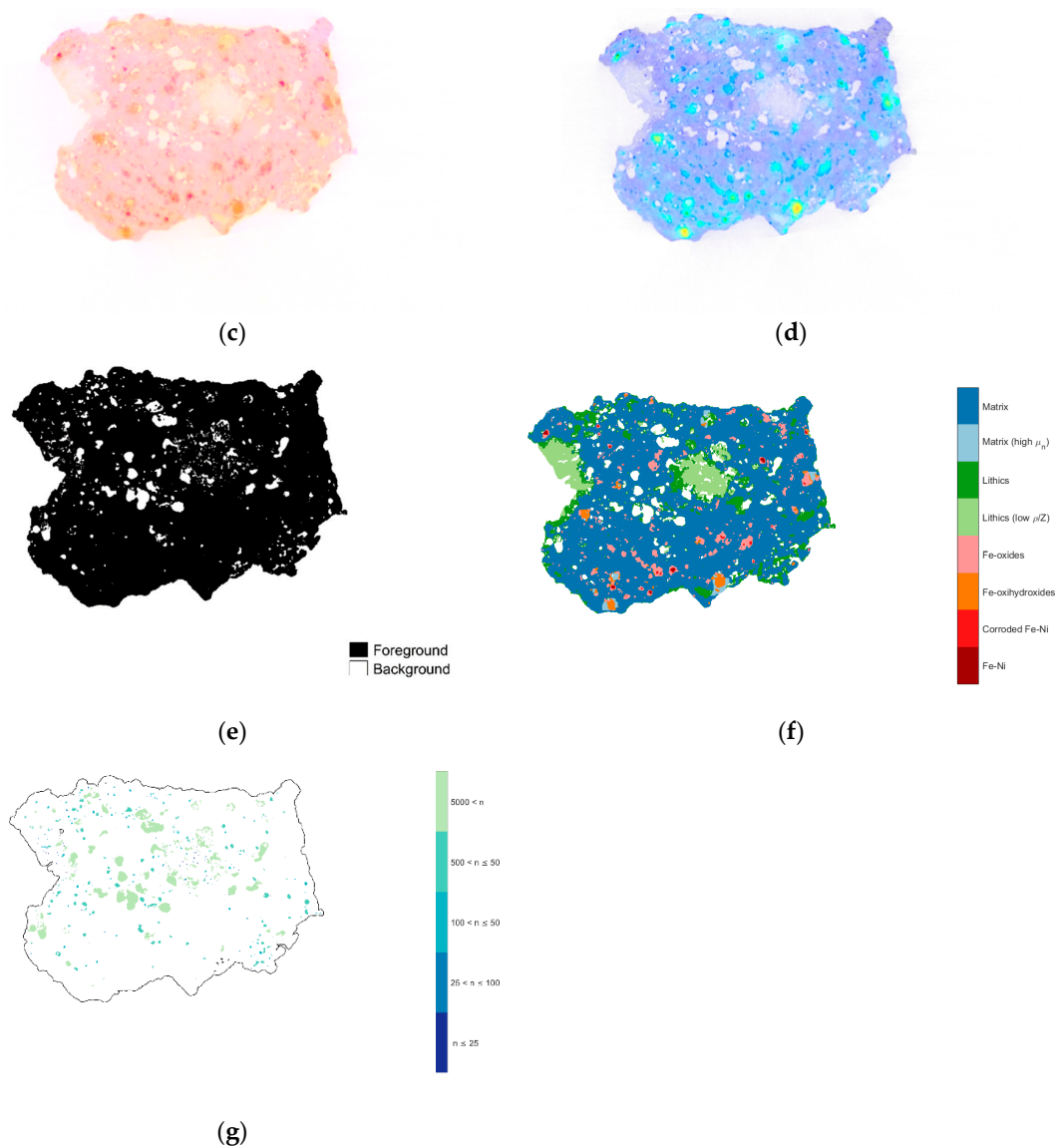


**Figure A2.** Impactite corresponding slices for  $z = 673$ . (a) X-ray volume; (b) neutron volume; (c) RGB false colour representation; (d) JET false colour representation; (e) mask selecting the impactite (foreground); (f) MRF segmentation; (g) vesicle distribution of the impactite.

Slice  $z = 913$ .

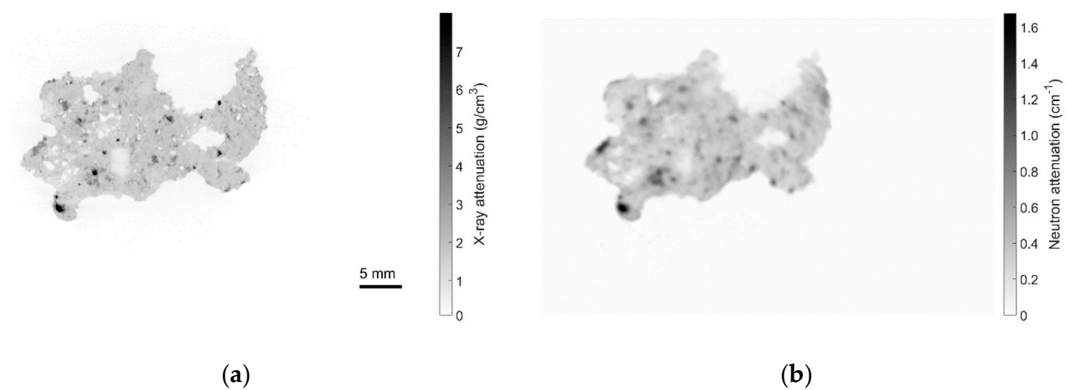


**Figure A3.** Cont.

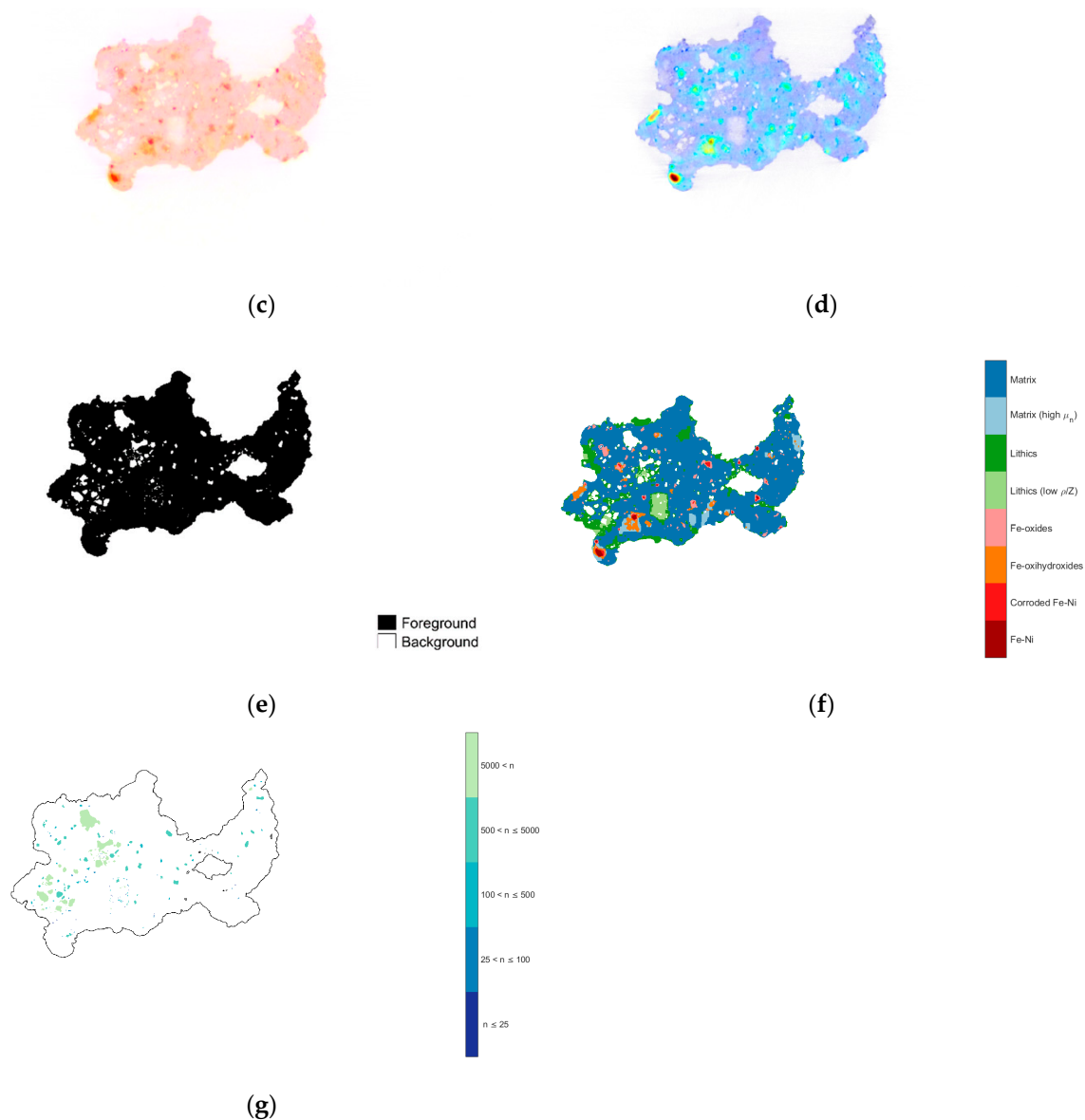


**Figure A3.** Impactite corresponding slices for  $z = 913$ . (a) X-ray volume; (b) neutron volume; (c) RGB false colour representation; (d) JET false colour representation; (e) mask selecting the impactite (foreground); (f) MRF segmentation; (g) vesicle distribution of the impactite.

**Table A1.** Density  $\rho$  ( $\text{g}/\text{cm}^3$ ) and linear neutron attenuation  $\mu$  ( $\text{cm}^{-1}$ ) values of the materials classes used for the MRF segmentation. The values were defined by selecting representative areas in the volume and calculating the corresponding mean X-ray and neutron attenuation values.

#	Class Colour	X-ray $\rho$ [ $\text{g}/\text{cm}^3$ ]	Neutron $\mu$ [ $\text{cm}^{-1}$ ]	Material
1	■	1.6	0.27	Matrix glass
2	■	1.5	0.73	Matrix (high neutron attenuation $\mu_n$ )
3	■	1.0	0.19	Lithic fragments
4	■	0.65	0.18	Lithic fragments (low $\rho/Z$ )
5	■	3.5	0.36	Iron oxides (dominantly maghemite)
6	■	3.15	1.20	Iron oxihydroxides (dominantly goethite)
7	■	5.2	0.80	Fe-Ni corroded spherules or containing troilite
8	■	7.8	0.82	Fe-Ni spherules



## References

1. Cifelli, R.L.; Lipka, T.R.; Schaff, C.R.; Rowe, T.B. First Early Cretaceous mammal from the eastern seaboard of the United States. *J. Vertebr. Paleontol.* **1999**, *19*, 199–203. [[CrossRef](#)]
2. Carlson, W.D.; Rowe, T.; Ketcham, R.A.; Colbert, M.W. Applications of high-resolution X-ray computed tomography in petrology, meteoritics and palaeontology. In *Geological Society; Special Publications*: London, UK, 2003; Volume 215, pp. 7–22.
3. Cnudde, V.; Boone, M.N. High-resolution X-ray computed tomography in geosciences: A review of the current technology and applications. *Earth-Sci. Rev.* **2013**, *123*, 1–17. [[CrossRef](#)]
4. Winkler, B. Applications of Neutron radiography and Neutron Tomography. *Rev. Mineral. Geochem.* **2006**, *63*, 459–471. [[CrossRef](#)]
5. Wilding, M.C.; Wilson, M.; McMillan, P.F. X-ray and neutron diffraction studies and MD simulation of atomic configurations in polyamorphic  $\text{Y}_2\text{O}_3\text{-Al}_2\text{O}_3$  systems. *Philos. Trans. R. Soc. A* **2005**, *363*, 589–607. [[CrossRef](#)] [[PubMed](#)]
6. Dierick, M.; Vlassenbroeck, J.; Masschaele, B.; Cnudde, V.; Van Hoorebeke, L.; Hillenbach, A. High-speed neutron tomography of dynamic processes. *Nucl. Instrum. Methods Phys. Res. A* **2005**, *542*, 296–301. [[CrossRef](#)]
7. Strobl, M.; Kardjilov, N.; Hilger, A.; Manke, I.; Banhart, J. Topical Review: Advances in neutron radiography and tomography. *J. Phys. D* **2009**, *42*, 243001. [[CrossRef](#)]
8. Kaestner, A.P.; Hovind, J.; Boillat, P.; Muehlebach, C.; Carminati, C.; Zarebanadkouki, M.; Lehmann, E.H. Bimodal Imaging at ICON Using Neutrons and X-rays. *Phys. Procedia* **2017**, *88*, 314–321. [[CrossRef](#)]
9. LaManna, J.M.; Hussey, D.S.; Baltic, E.; Jacobson, D.L. Neutron and X-ray Tomography (NeXT) system for simultaneous, dual modality tomography. *Rev. Sci. Instrum.* **2017**, *88*, 113702. [[CrossRef](#)] [[PubMed](#)]
10. Teganini, A.; Atkins, D.; Giroud, B.; Ando, E.; Beaucour, J.; Viggiani, G. NeXT-Grenoble, a novel facility for Neutron and X-ray Tomography in Grenoble. In *Proceedings of the 3rd International Conference on Tomography of Materials and Structures*, Lund, Sweden, 26–30 June 2017.
11. Banhart, J. *Advanced Tomographic Methods in Materials Research and Engineering*; Oxford University Press: Oxford, UK, 2008.
12. Fettes, D.; Desmons, J. (Eds.) *Metamorphic Rocks: A Classification and Glossary of Terms*; Cambridge University Press: Cambridge, UK, 2007.
13. Echaurren, J.C.; Ocampo, A.C.; Rocca, M.C.L. A Mathematical model for the Monturaqui Impact Crater, Chile, South America, Meteoritics & Planetary Science 40, Supplement. In *Proceedings of the 68th Annual Meteoritical Society Meeting of the Meteoritical Society*, Gatlinburg, TN, USA, 12–16 September 2005; p. 5004.
14. Evans, N.J.; Gregoire, D.C.; Grieve, R.A.F.; Goodfellow, W.D.; Veizer, J. Use of platinum-group elements for impactor identification: Terrestrial impact craters and Cretaceous-Tertiary boundary. *Geochim. Cosmochim. Acta* **1993**, *57*, 3737–3748. [[CrossRef](#)]
15. Ebert, M.; Hecht, L.; Deutsch, A.; Kenkmann, T. Chemical modification of projectile residues and target material in a MEMIN cratering experiment. *Meteorit. Planet. Sci.* **2013**, *48*, 134–149. [[CrossRef](#)]
16. Hamann, C.; Hecht, L.; Ebert, M.; Wirth, R. Chemical projectile–target interaction and liquid immiscibility in impact glass from the Wabar craters, Saudi Arabia. *Geochim. Cosmochim. Acta* **2013**, *121*, 291–310. [[CrossRef](#)]
17. French, B.M.; Koeberl, C. The Convincing Identification of Terrestrial Meteorite Impact Structures: What Works, What Doesn't and Why. *Earth-Sci. Rev.* **2010**, *98*, 123–170. [[CrossRef](#)]
18. Ukstins Peate, I.; van Soest, M.; Wartho, J.; Cabrol, N.; Grin, E.; Piatek, J.; Chong, G. A Novel Application of (U-Th)/He Geochronology to Constrain the Age of Small, Young Meteorite Impact Craters: A Case Study of the Monturaqui Crater, Chile. In *Proceedings of the 41st Lunar and Planetary Science Conference*, Houston, TX, USA, 1–5 March 2010.
19. Sanchez, J.; Cassidy, W. A previously undescribed meteorite crater in Chile. *J. Geophys. Res.* **1966**, *70*, 4891–4895. [[CrossRef](#)]
20. Hartley, A.J.; Chong, G.; Houston, J.; Mather, A.E. 150 million years of climatic stability: Evidence from the Atacama Desert, northern Chile. *J. Geol. Soc.* **2005**, *162*, 421–424. [[CrossRef](#)]
21. Ugalde, H.; Valenzuela, M.; Milkereit, B. An integrated geophysical and geological study of the Monturaqui impact crater, Chile. *Meteorit. Planet. Sci.* **2007**, *42*, 2153–2163. [[CrossRef](#)]

22. Ramirez, C.F.; Gardeweg, M. *Hoja Toconao, Region de Antofagasta*; Servicio Nacional de Geología y Minería: Santiago, Chile, 1982.
23. Bunch, T.E.; Cassidy, W.A. Petrographic and electron microprobe study of the Monturaqui impactite. *Contrib. Mineral. Petrol.* **1972**, *36*, 95–112. [[CrossRef](#)]
24. Lipka, J.; Madsen, M.B.; Koch, C.B.; Miglierini, M.; Knudsen, J.M.; Morup, S. The Monturaqui impactite and the iron in it. *Meteoritics* **1994**, *29*, 492.
25. Gibbons, R.V.; Hörz, F.; Thompson, T.D.; Brownlee, D.E. Metal spherules in Wabar, Monturaqui, and Henbury impactites. In Proceedings of the 7th Lunar and Planetary Science Conference, Houston, TX, USA, 15–19 March 1976; pp. 863–880.
26. Koch, C.B. Weathering of impactite from Monturaqui. *Program Abstr. Clay Miner. Soc.* **1991**, 91.
27. Koch, C.; Buchwald, V.F. Weathering of Iron Meteorites from Monturaqui, Chile. *Meteoritics* **1994**, *29*, 443.
28. Kearsley, A.; Graham, G.; McDonnell, T.; Bland, P.; Hough, R.; Helps, P. Early fracturing and impact residue emplacement: Can modelling help to predict their location in major craters? *Meteorit. Planet. Sci.* **2004**, *39*, 247–265. [[CrossRef](#)]
29. Klobberdanz, C.M. Geochemical Analysis of the Monturaqui Impact Crater, Chile. Master's Thesis, University of Iowa, Iowa City, IA, USA, 2010.
30. Cukierski, D.O. Textural and Compositional Analysis of Fe-Ni Metallic Spherules in Impact Melt from Monturaqui Crater, Chile. Unpublished Master's Thesis, University of Iowa, Iowa City, IA, USA, 2013. Available online: <https://ir.uiowa.edu/cgi/viewcontent.cgi?article=4595&context=etd> (accessed on 12 May 2018).
31. Ikeda, Y.; Kojima, H. Terrestrial alteration of Fe-Ni metals in Antarctic ordinary chondrites and the relationships to their terrestrial ages. *Proc. NIPR Symp. Antarct. Meteor.* **1991**, *4*, 307–318.
32. Jackson, D.F.; Hawkes, D.J. X-ray attenuation coefficients of elements and mixtures. *Phys. Rep.* **1981**, *70*, 169. [[CrossRef](#)]
33. Jenkins, R.; Snyder, R.L. *Introduction to X-ray Powder Diffractometry*; John Wiley: New York, NY, USA, 1996.
34. Vlassenbroeck, J.; Cnudde, V.; Masschaele, B.; Dierick, M.; van Hoorebeker, L.; Jacobs, P. A comparative and critical study of X-ray CT and neutron CT as non-destructive material evaluation techniques. *Geol. Soc.* **2007**, *271*, 277–285. [[CrossRef](#)]
35. Kak, A.C.; Slaney, M. *Principles of Computerised Tomographic Imaging*; IEEE Press: New York, NY, USA, 1988.
36. Cormack, A.M. Representation of functions by its line integrals with some radiological applications. *J. Appl. Phys.* **1963**, *34*, 2722. [[CrossRef](#)]
37. Hounsfield, G.N. Computerized transverse axial scanning (tomography). *Br. J. Radiol.* **1973**, *46*, 1016. [[CrossRef](#)] [[PubMed](#)]
38. Ott, F.; Loupiac, C.; Désert, S.; Hélar, A.; Lavie, P. IMAGINE: A cold neutron imaging station at the Laboratoire Léon Brillouin. *Phys. Procedia* **2015**, *69*, 67–70. [[CrossRef](#)]
39. Inside Matters. Octopus. 2017. Available online: <https://octopusimaging.eu/octopus/octopus-reconstruction> (accessed on 1 October 2017).
40. Deans, S.R. *The Radon Transform and Some of Its Applications*; Courier Corporation: North Chelmsford, MA, USA, 2007.
41. Schindelin, J.; Arganda-Carreras, I.; Frise, E.; Kaynig, V.; Longair, M.; Pietzsch, T.; Preibisch, S.; Rueden, C.; Saalfeld, S.; Schmid, B.; et al. Fiji: An open-source platform for biological-image analysis. *Nat. Methods* **2012**, *9*, 676–682. [[CrossRef](#)] [[PubMed](#)]
42. Penny, W.D.; Ashburner, J.; Kiebel, S.; Henson, R.; Glaser, D.E.; Phillips, C.; Friston, K. Statistical Parametric Mapping: An Annotated Bibliography. 2001. Available online: <http://www.fil.ion.ucl.ac.uk/spm/software/spm8/> (accessed on 1 October 2017).
43. Collignon, A.; Maes, F.; Delaere, D.; Vandermeulen, D.; Suetens, P.; Marchal, G. Automated Multi-modality Image Registration Based On Information Theory. In *Proceedings of Information Processing in Medical Imaging*; Bizais, Y., Barillot, C., Di Paola, R., Eds.; Kluwer Academic Publishers: Dordrecht, The Netherlands, 1995.
44. Studholme, C.; Hill, D.L.; Hawkes, D.J. An overlap invariant entropy measure of 3D medical image alignment. *Pattern Recognit.* **1999**, *32*, 71–86. [[CrossRef](#)]
45. Viola, P.; Wells, W.M., III. Alignment by maximization of mutual information. In *Proceedings of the International Conference on Computer Vision, Cambridge, MA, USA, 20–23 June 1995*; Grimson, E., Shafer, S., Blake, A., Sugihara, K., Eds.; IEEE Computer Society Press: Los Alamitos, CA, USA, 1995; pp. 16–23.

46. Otsu, N. A Threshold Selection Method from Gray-Level Histograms. *IEEE Trans. Syst. Man Cybern.* **1979**, *9*, 62–66. [[CrossRef](#)]
47. Li, S.Z. *Markov Random Field Modeling in Image Analysis*; Springer: Berlin, Germany, 2009.
48. Brett, R. Metallic spherules in impactite and tektite glasses. *Am. Miner.* **1967**, *52*, 721–733.



© 2018 by the authors. Licensee MDPI, Basel, Switzerland. This article is an open access article distributed under the terms and conditions of the Creative Commons Attribution (CC BY) license (<http://creativecommons.org/licenses/by/4.0/>).